ELSEVIER

The reaction of O_2 with Al(1 1 0): a medium energy ion scattering study of nano-scale oxidation

D. Starodub [a,*], T. Gustafsson [a], E. Garfunkel [b]

[a] *Department of Physics and Astronomy, Rutgers University, 136 Frelinghuysen Road, Piscataway, NJ 08854-8019, USA*
[b] *Department of Chemistry, Rutgers University, Piscataway, NJ 08854-8087, USA*

Abstract

We have used medium energy ion scattering to study oxygen transport and oxidation kinetics of Al(1 1 0) at elevated temperatures in dry oxygen. Oxidation results in the formation of a stable stoichiometric Al_2O_3 layer with fairly abrupt interfaces. The time dependence of the film growth follows inverse logarithmic law, in agreement with the Cabrera–Mott (field-assisted) oxidation mechanism. The dependence of the growth rate on pressure is parabolic. Microscopic details on oxidation mechanism are studied by re-oxidizing a thin oxide layer with isotopically labeled oxygen. The depth profiling of oxygen traces in the oxide shows that oxygen ions are mobile species transported via migration of oxide network defects. This migration across the film is the rate-limiting step controlling oxidation.
© 2004 Elsevier B.V. All rights reserved.

Keywords: Medium energy ion scattering (MEIS); Oxidation; Aluminum

1. Introduction

It is generally accepted that the growth of ultra-thin (<30 Å) metal oxide films is described by the Cabrera–Mott oxidation mechanism [1]. In this model, electrons tunnel freely from a metal to an adsorbed oxygen atom through a dielectric film in order to equalize the electrochemical potential. This creates an electric field across the film, which in turn makes possible atomic transport to the interface where the oxidation reaction occurs. The crucial role of the electric field and the ionic nature of material transport in this process are well established experimentally, in particular, for aluminum oxide. Negative surface bias with respect to the substrate is shown to enhance oxidation, while positive bias reduces the oxidation rate [2]. The growth rate can also be accelerated by electron bombardment [3,4], establishing a larger electric field due to the increased charge on the surface. The effect of the electric field on the oxidation kinetics is supported by faster growth in ozone compared to in oxygen [5], which can be related to the higher electrostatic potential across the film because of the larger electron affinity of ozone. Information about the electric field across the oxide film produced by the deposition of high electron affinity species (Au, O_3, NO_2, Cl_2) or

---
* Corresponding author. Tel.: +1-732-445-3926; fax: +1-732-445-4991.
   E-mail address: starodub@physics.rutgers.edu (D. Starodub).

electron bombardment has been derived from the change in the energy position and shape of the oxidic Al^{3+} 2p peak in the X-ray photoemission spectra [6–8]. Although most previous workers agree that field-enhanced diffusion is real, the details of the atomic transport across aluminum oxide remain a subject of controversy. Most studies on aluminum oxidation have been primarily concerned with the growth kinetics, which alone does not yield an unambiguous conclusion about the oxidation mechanism. Further insight can be obtained by tracing the evolution of marker species [9] (inert atoms or metal/oxygen atoms) during oxidation. Results are scarce in the oxide thickness range of interest, since few experimental techniques are capable of providing sufficient depth resolution for films several nm thick. Finally, aluminum oxidation is slow due to the low concentration and mobility of defects (which facilitate material transport across the film) and thus it is difficult to follow the precise mechanism.

In the original formulation of Cabrera and Mott [1] the migrating species is a metal interstitial, injected at the oxide–metal interface. Later, the possibility of surface-injected oxygen transport was proposed [10], as well as vacancy transport, place exchange, etc. Generally it is assumed that oxide morphology (phase and crystallinity) and bond strength determine the transport mechanism [11]. Oxides with strong bonds (such as SiO_2), which form random open networks with a high degree of short range order, are more permeable to larger anions, while in compact oxides with weak bonds the transport is provided by the smaller cations. Aluminum oxide occupies an intermediate position in the bond strength hierarchy. Therefore aluminum ions, oxygen ions, or some combination of the two have been suggested as the mobile species in Al_2O_3. The nature of migrating species may also vary for different oxidation conditions, which affect the defect structure of the oxide. For example, Al anodization studies [12,13] demonstrate a strong dependence of the metal to oxygen transport ratio on electrolyte type and anodization current. In the case of dry oxygen oxidation, the oxygen vacancy concentration in the oxide network can be varied by changing the growth conditions [6]. The rate of oxidation was found to be higher for an oxide enriched in oxygen vacancies, i.e. with a low oxygen to aluminum stoichiometric ratio. The mobile species in such an oxide was likely oxygen atoms. However, the transport mechanism may well be different for stoichiometric aluminum oxide. Studies of the growth of crystalline oxide islands beneath an amorphous oxide film [14] during oxidation above 620 K suggest oxygen permeation through this film. On the other hand, interface incorporated Al interstitials [2,15] and surface incorporated Al vacancies [16] have also been proposed as migrating species. Ionic transport can be greatly modified by the presence of extended defects, such as dislocations and grain boundaries in crystalline oxides or channels in amorphous oxides. In many cases water vapor was used as oxidant [3,16,17]. Though such oxidation is important from a practical point of view, interpretation of the data becomes more complicated, as hydroxyl groups, incorporated into the oxide, modify its defect structure and therefore affect the transport mechanism [18].

In this paper we address the microscopic details of the initial oxidation by a combined study of the kinetic and microscopic processes in the simplest case to analyze, namely thermal oxidation of an aluminum single crystal in molecular (dry) oxygen. At moderate temperatures (<600 K), oxidation results in the growth of a thin (<30 Å) [19] amorphous film. At higher temperatures and thickness there is a tendency for the film to crystallize [20] into γ-Al_2O_3, potentially involving new transport routes, such as crystalline grain boundaries. Thermodynamic calculations [21] show that crystallization (of an amorphous oxide overlayer) is less likely to occur on Al(1 1 0) relative to the other low index surfaces.

2. Experimental

2.1. Experimental technique

We have used medium energy ion scattering (MEIS) to provide a quantitative depth-resolved compositional analysis of the film structure. The strength of MEIS is that it is a well established, quantitative technique [22], with a depth resolu-

tion in the near surface region significantly better than 1 nm. The measurements have been performed in a UHV analytical chamber with a base pressure of 1×10^{-10} Torr, in conjunction with a 400 keV ion accelerator. Collection and energy/angle separation of the scattered ions is performed by a high-resolution toroidal electrostatic energy analyzer [23] equipped with micro-channel plates and a 2D position sensitive detector. The energy resolution is 0.2% and the angular resolution is about 0.4°. Auxiliary equipment includes a LEED system to monitor the long range order of the clean Al(1 1 0) surface.

We used a 98.0 keV incident proton beam. The energy of a particle scattered at the surface is related to the incident energy by a kinematic factor. This kinematic factor is a consequence of classical energy and momentum conservation, and depends on the scattering angle and target mass. That makes MEIS a mass-sensitive technique. As a proton travels inside the sample, it loses energy to electronic excitations [22,24]. This results in the additional energy shift of the scattered projectile, proportional to the path length in the solid. Thus, a depth profile of the elements in the target can be extracted from the energy distribution of the scattered particles. To minimize the background for the oxygen signal located at lower energies, the scattering from the sub-surface (crystalline) aluminum substrate must be suppressed. This is achieved by employing a specific channeling and blocking scattering geometry, where the incident proton beam and detector are aligned with major crystallographic directions of the target. Then for an ideal frozen lattice only the topmost atoms of the crystalline substrate will contribute to the scattered signal. In practice, due to thermal vibrations and shift of atoms from their ideal lattice positions, a few sub-surface atomic layers are partially visible to the detector. Due to the random distribution of O and Al atoms in the amorphous oxide overlayer, their visibility to incident ions is not reduced in the channeling and blocking geometry. Therefore, the increase of the O and Al peak areas during oxidation can be directly related to the oxide content. All measurements have been done for a scattering angle of 120°, with the incident proton beam normal to the surface, and the

detector placed in the [0 1 1] direction. For better statistics, the scattering data have been summed up in an angular range of 2°. In preliminary experiments, we observed radiation damage, which appears as increased background from the Al substrate, for irradiation doses exceeding 3×10^{17} protons/cm^2. Therefore, the beam position on the sample was changed after 15% of this dose had been accumulated.

2.2. Neutralization measurements

The area under a MEIS peak can be converted into an areal density of the target element, provided the scattering cross-section and the charged fraction of the scattered projectiles are known. We use cross sections obtained from the Molière potential, a screened Coulomb potential [25]. This gives a good approximation for protons in the 100 keV range. The major source of error in the calculation of the elemental areal densities is the uncertainty in the knowledge of the charged fraction of the backscattered protons. O'Connor et al. [26] have reported a decrease of the charged fraction of 100 keV protons, scattered on Al(1 1 1), from 92% to 86% as the oxygen coverage increased from 0 to 0.5–0.7 monolayers. To determine the charged fraction of the scattered protons, we employed a surface barrier detector (SBD) with fairly poor energy resolution. By removing the charged particles with an electric field, we detected the neutral fraction of the scattered projectiles. We found a proton charged fraction of 89% for the clean Al(1 1 0) surface and 77% for oxide films with thickness ranging from 8 to 20 Å. The low SBD resolution did not allow us to measure the energy dependence of the charged fraction. To take this into account we used the empirical energy dependence of the charged fraction for oxidized Al [27]. This dependence fits well the measured value for 98 keV incident protons.

2.3. Sample preparation and oxidation procedure

A commercially manufactured Al crystal with (1 1 0) orientation was electropolished in a solution of perchloric acid and acetic anhydride. After mounting the sample in the UHV chamber, it was

cleaned by several cycles of sputtering with 1.0 keV Ne^+ ions and sequential annealing, until a (1×1) LEED pattern could be observed, and no carbon, oxygen and heavy element contamination could be detected by MEIS. The sample was heated from behind by a tungsten filament. The temperature was monitored by a chromel–alumel thermocouple, attached to the rim of the sample.

A difficulty in MEIS with the type of analyzer we use is the influence of oxygen adsorption on the efficiency of the channel plates [28]. The sample was therefore oxidized in a separate chamber (base pressure of 8×10^{-11} Torr) connected through an interlock to the analysis chamber. To monitor the location of oxygen incorporated and redistributed during thermal treatment, a two-step isotopic oxidation procedure was performed, using ^{16}O and then ^{18}O-enriched (or vice versa) dry oxygen gas (O_2). We will refer to the first-grown oxide (with ^{16}O) as the marker film, and the oxygen used in the second step as the tracer. Research grade (99.998%) $^{16}O_2$ gas with the natural ^{16}O abundance (99.76%) was used. The $^{18}O_2$ gas had an isotopic enrichment of 99%. A mass-spectrometric analysis of its composition, performed in the oxidation chamber, revealed the presence of 0.1% of $H_2^{16}O$ and 0.2% of $C^{16}O$ and $C^{16}O_2$ combined (which may result from cracking in the mass spectrometer or reactions on the chamber wall). To prevent sample bombardment by electrons, all hot filaments (except the sample heater) were turned off during oxidation. The oxygen pressure was controlled by a Pirani gauge calibrated against an ion gauge in an oxygen environment.

3. Results

The marker film was grown at room temperature (RT) and a pressure of 10^{-3} Torr. Under these conditions, the film thickness saturates at ca. 8 Å, as measured by MEIS, after 10–15 min of oxidation. This film is stable under 30 min vacuum anneal at 573 K. Two series of re-oxidation cycles, aimed at examining the time and pressure dependence of the oxide growth, were conducted. To study the time dependence, the sample was first exposed to $^{16}O_2$, and re-oxidation was then carried
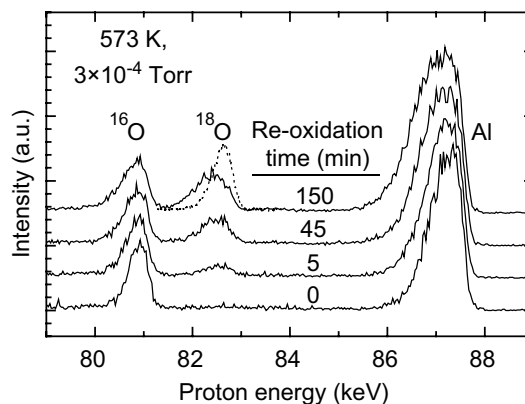
Fig. 1. Evolution of the MEIS spectra during re-oxidation of Al(1 1 0) surface covered with thin $Al_2^{16}O_3$ film in $^{18}O_2$ under conditions indicated in the figure. The dotted line is the ^{18}O peak for a homogeneous $Al_2^{18}O_3$ film.

out in $^{18}O_2$ at a pressure of 3×10^{-4} Torr and temperatures of 573 and 673 K. Two oxidation series have been performed, both starting with a clean Al surface, and the oxide thickness was measured after each oxidation step. The MEIS spectra taken after the first step oxidation and several re-oxidation steps at 573 K are presented in Fig. 1. Upon saturation at RT the spectrum is characterized by a surface Al peak and a ^{16}O peak from the oxide layer. Subsequent exposure to $^{18}O_2$ results in appearance of an additional peak characteristic of ^{18}O with area proportional to amount of incorporated oxygen. The kinetic data are shown in Fig. 2. The dashed line shows an attempt
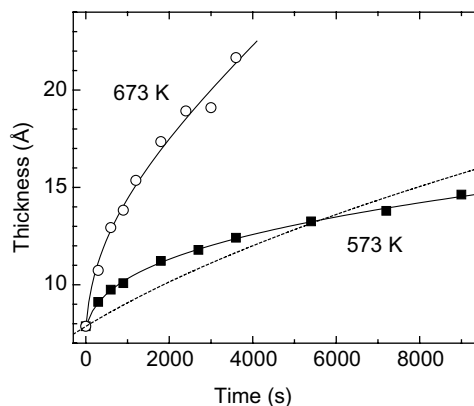
Fig. 2. Growth of Al_2O_3 oxide for two temperatures. Solid lines are to guide the eye, dash line is a fit to the parabolic law.

to fit the time dependence of the oxide layer thickness at 573 K to a parabolic rate law ($X^2 \propto t$), corresponding to the slowest step in the oxidation process being diffusion governed by the gradient of the electrochemical potential. Since the experimental curve exhibits a tendency to saturation, this fit is clearly not satisfactory, and therefore we will explore oxidation kinetics described by logarithmic-type rate laws as explained below. Unfortunately, it was not possible to measure the kinetics of oxidation at 673 K for longer times because of the development of significant roughness of the oxide layer. Detailed information about the isotopic distribution in the oxide layer follows from shape and position of the O peaks. As an example, a comparison in Fig. 1 of the ^{18}O peak upon 150 min re-oxidation in $^{18}O_2$ with that for ^{18}O forming a uniform surface oxide film after exposure of a clean Al(1 1 0) surface to $^{18}O_2$ (dotted line) clearly reveals a very different shape at similar total area (concentration). A broader energy distribution, a slight shift towards lower energy and a less steep slope of the front edge for the former peak indicate that upon re-oxidation isotopic intermixing, which is non-uniform in depth, occurs. To measure the pressure dependence of the oxidation, $^{18}O_2$ gas was used to form a marker film, and re-oxidation (in $^{16}O_2$) then took place for 15 min at different pressures. This oxidation sequence is preferable to measure a possible loss of oxygen from oxide, since it cannot be masked by incorporation of ^{18}O-containing impurities during second-stage oxidation in $^{16}O_2$. Fig. 3 shows MEIS energy spectra recorded upon re-oxidation at 673 K. A pressure dependence of the oxidation rate is clearly observed from the change of the ^{16}O area with pressure. The ^{18}O peak broadens dramatically during re-oxidation, which can be attributed to a place exchange reaction with newly incorporated oxygen. The reduction of the ^{18}O area indicates oxygen loss into the gaseous phase. At the same time, the maximum of the ^{18}O peak shifts only insignificantly towards lower energy, implying that the maximum in the ^{18}O depth distribution remains at the surface. This behavior is reflected in the shape of the ^{16}O peak. For higher oxidation pressures, a distinct surface ^{16}O intensity reduction, as compared to that expected for a uniform film, is indi-
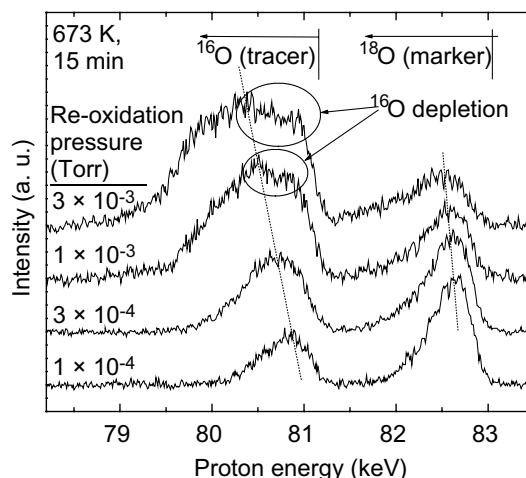
Fig. 3. Oxygen MEIS spectra upon re-oxidation of thin Al$_2$^{18}O$_3$ film in $^{16}O_2$ at various pressures.

cated in Fig. 3. As a result, the maximum of the ^{16}O peak for high pressures shows a significant shift to lower energies, and is located in central part of the peak. This corresponds to the permeation of oxygen ions through a relatively stable surface marker film and preferential oxide build up at the oxide–metal interface. The observed isotopic distributions can be explained only by assuming that the oxygen ions are the mobile species responsible (at least in part) for material transport during oxidation.

4. Theory of oxidation kinetics in ultra-thin films

The oxide thickness range of interest (from 5 to 30 Å) is well below the typical width of a space-charged layer. Therefore, space charge can be ignored, and the electric field across the oxide (established only by the surface charges on the gas–oxide and oxide–metal interfaces) can be considered as uniform. Furthermore, electronic and ionic currents accompanying growth can be considered independently. The mechanism of electron/hole tunneling through the oxide layer is very efficient for films thinner than 30 Å, establishing an electronic current equilibrium. Under these assumptions, the potential drop across the film $\Delta\varphi$ equals the difference between the metal

work function and the affinity level of chemisorbed oxygen (which is the sum of the oxygen affinity and the oxygen atom binding energy). The electric field set up by this potential provides a driving force for slow ion incorporation and/or transport. Note that this transport occurs in a non-equilibrium system, and therefore cannot be described by the gradient of the electrochemical potential. Two types of oxidation kinetics can occur in this case depending on the mechanism of ionic transport (which in turn is determined by the oxide morphology). The general expression for a potential barrier to be overcome for a field-assisted jump of an ion between two adjacent sites can be written as [11]

$$W = W_0 - qaE + \lambda X, \tag{1}$$

where q is the ionic charge, $2a$ is the jump length, λ is a structural term, and X is the oxide thickness. The intrinsic barrier for an ion jump is W_0. The second term describes the lowering of W by an electric field E across the oxide, and the third term takes into account the blocking of extended defects as the film thickens.

Provided the potential difference across the film $\Delta\varphi$ is constant, the increase of the film thickness X reduces the electric field $E = \Delta\varphi/X$ in the oxide. If the ion movement takes place by generation of point defects, such as vacancies or interstitials, the third term in Eq. (1) can be neglected, and the change in the activation energy $\Delta W = W - W_0$ for ion movement is inversely proportional to X: $\Delta W = -qa\Delta\varphi/X$. The approximate solution of the resulting growth equation gives an inverse logarithmic dependence of the thickness on time t [1]:

$$\frac{x_1}{X} = -\ln\left(\frac{t}{X^2}\right) - \ln(x_1 u), \tag{2a}$$

where x_1 and u are constants determined by physical parameters of the system:

$$u = N\Omega v \exp\left(-\frac{W_0}{T}\right), \tag{2b}$$

$$x_1 = \left|\frac{qa\Delta\varphi}{T}\right|. \tag{2c}$$

Herein v is a lattice vibration frequency of the order of 10^{12} s^{-1}, T is the oxidation temperature, N is the areal density of the potentially mobile species, and Ω is the oxide volume per incorporated oxygen (aluminum) ion.

The validity of Eq. (2a) can be tested by plotting $1/X$ as a function of $\ln(t/X^2)$. A straight line with a slope defined by $\Delta\varphi$ should be obtained. The values of N and W_0 can be extracted from an Arrhenius plot of u.

An alternative microscopic mechanism for ion movement is via extended defects in the oxide layer, such as structural channels or, for polycrystalline films, grain boundaries. As the film grows, these easy pathways for ion migration gradually become blocked by the formation of oxide within them [29]. Also, their characteristic length can become small with respect to the layer thickness, slowing the rate of ion motion. Thus, though the activation energy is again larger for thicker films, its change is directly proportional to the oxide thickness, provided $X^2 > qa\Delta\varphi/\lambda$ or in case of a thickness independent electric field: $\Delta W = \lambda X$. Then the exact solution of the growth equation is direct logarithmic kinetics with a linear dependence of X on $\ln(t)$:

$$X = \frac{T}{\lambda} \ln[1 + \xi(T) \cdot t], \tag{3}$$

where $\xi(T)$ is defined by the system parameters.

A direct logarithmic law also results if oxidation is rate-limited by electron tunneling [18].

5. Discussion

5.1. Film characterization: stoichiometry and interface structure

From an ion scattering point of view all the Al nuclei in a random oxide network contribute equally to the scattering signal. Due to channeling/blocking only the top atomic layer and fractions of a few sub-surface layers of the crystalline Al substrate are visible to the detector. As the oxide grows, the oxygen atoms form bonds with aluminum atoms and displace them from their lattice sites. The displaced Al atoms can now become visible to the ion beam and be detected. Therefore, the Al signal will increase upon oxidation. If a stoichiometric amorphous Al_2O_3 oxide is formed,

the incorporation of three oxygen atoms into the oxide network should be accompanied by an increase of the Al yield by two atoms. The slope of a plot of the areal density of visible Al atoms as a function of O coverage (areal density) gives the number of displaced Al atoms per O atom in the oxide. From this, the stoichiometry of the oxide can be determined (Fig. 4(a)). A straight line with a slope of 2/3 (solid line), corresponding to the stoichiometric oxide, is within the error of the least-square linear fit (dashed line). This implies growth of stoichiometric Al_2O_3 for film thicknesses ranging from 8 to 15 Å. Extrapolation of this line to zero oxide thickness (O coverage) gives an intercept for the Al yield of 0.349 Å^{-2}. The experimentally measured Al signal for a clean Al(1 1 0) surface in this geometry is 0.313 Å^{-2}. There is therefore some 0.036 Å^{-2} to be accounted for. Assuming an Al density of 2.7 g/cm^3, the excess in the measured Al yield corresponds to an effective 0.6 Å thick layer of displaced Al, which is less than one interlayer distance (1.432 Å) for Al(1 1 0). That amount can be due to lateral stress in the substrate layers and/or changes in the topmost Al(1 1 0) layer from relaxation introduced by the oxide.

The above considerations permit a partial determination of the interface composition and structure, but they are not sensitive to larger scale (involving lateral distances of more than several atomic spacings) interface roughness. For instance, a simple peak area intensity analysis does not allow us to distinguish between oxide growth by means of a uniform increase of the film thickness and in-depth island growth with subsequent lateral expansion underneath a thin continuous surface oxide film. The latter growth mode has been reported [14] for Al oxidation at temperatures above 620 K. This type of information can be obtained by taking into account the evolution of the Al and O peak widths (not simply the area) with oxide growth. The interface morphology is reflected in the peak shape, which can be characterized numerically at one level by the root mean square width [28]. In the case of a Gaussian distribution, the rms width is just twice the standard deviation σ. Interface/surface roughening (or island formation) would result in a rise of the low-
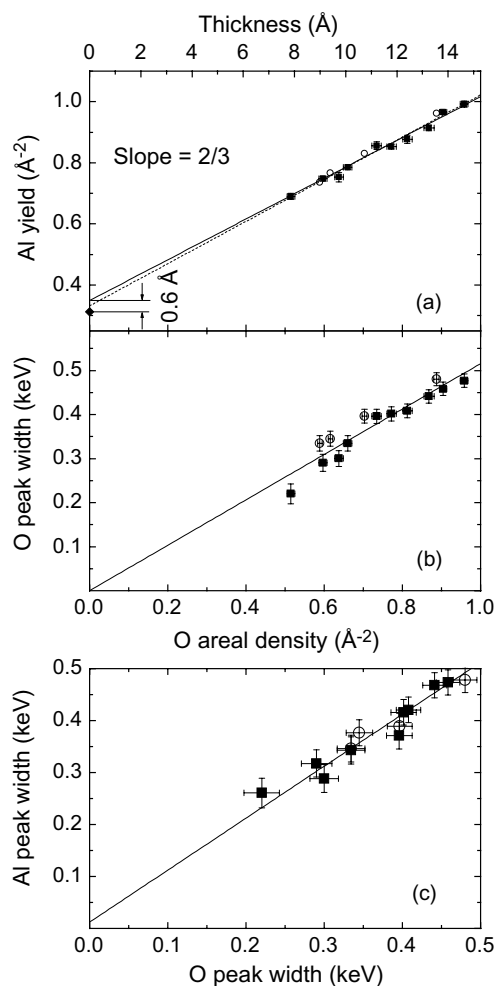
Fig. 4. (a) Visible Al yield as a function of O coverage. The best linear fit (slope = 0.69 ± 0.03) is shown by the dashed line. The solid line is the linear fit with a fixed slope of 2/3 corresponding to a stoichiometric Al_2O_3. The diamond shows the measured Al yield for the clean Al surface. (b) O peak width as a function of O coverage, and the least-square linear fit through origin; (c) Al peak width as a function of O peak width; the slope of the fitting straight line is 1. For all plots, filled symbols stand for films grown at fixed pressures, open at fixed time.

energy tail and an increase of the rms peak width. Fig. 4(b) shows the dependence of the O peak width w_O on O coverage. Because oxidation has been performed in two sequential steps using different O isotopes, the O peak width is calculated as the sum of the ^{16}O and ^{18}O peak widths weighted by their fraction in the overall O yield. A

correction was also applied to account for the instrumental resolution and the average peak broadening due to straggling, using the relationship $w_O = \sqrt{W_O^2 - (2 \cdot \sigma)^2}$, where W_O is the O peak width calculated from the spectra and $\sigma = 0.18$ keV. The data points lie on a straight line within the error bars. The limiting case of lateral island growth would result in a constant O peak width. In-depth growth of islands would lead to a faster penetration of oxygen atoms into the substrate (as compared to the thickening of a homogeneous flat film) at the same oxygen uptake rate. Therefore this situation would yield a faster increase of O peak width with coverage. The observed linear dependence can be associated with homogeneous in-depth growth without interface/surface roughening (the surface remains flat with, in effect, layer-by-layer oxidation of the substrate). The zero intercept implies a flat oxide-metal interface. Fig. 4(c) presents a plot of the Al peak width w_{Al} as a function of the O peak width. The former is defined as $w_{Al} = \sqrt{W_{Al}^2 - (2 \cdot \sigma)^2} - \sqrt{W_{Al}^2(0) - (2 \cdot \sigma)^2}$ in order to exclude the instrumental resolution and the contribution from the Al substrate. Here W_{Al} is the Al peak width from the measured spectrum, and $W_{Al}(0)$ is the Al peak width for zero oxygen coverage, experimentally measured to be 0.48 keV. A straight line as shown in Fig. 4(c) fits the resulting dependence of the Al peak width vs. the width of the O peak. The fact that the slope is equal to 1 implies that both O and oxidized Al expand into the substrate at the same rate. As expected for a uniform flat film, extrapolation to a zero oxygen peak width gives to a good approximation a zero intercept.

In order to check for roughness, we sometimes collected additional spectra at a scattering angle of 60°, with the incident beam impinging along the $[\bar{1}\,0\,1]$ orientation, and with the detector aligned along the [0 1 1] direction. This tilted incident beam makes the data for this configuration more sensitive to surface and/or interface roughness. We have been able to fit the energy spectra (see Section 5.3) for both scattering geometries using the same model of the elemental distributions with an abrupt oxide–metal interface. This indicates insignificant surface/interface roughness.

Thus, Al(1 1 0) oxidation at 573 K results in the growth of a uniform stoichiometric Al_2O_3 film with both microscopic and macroscopic interface features not deviating by more than one atomic layer of Al from ideal (homogeneous flat layer) growth.

The situation changes for oxidation at 673 K. For a pressure exceeding 10^{-3} Torr, the measured spectra could not be fit to a model with a flat oxide–metal interface. In this case the O and Al peaks exhibited slightly longer (as compared to simulations) low-energy tails, attributed to the onset of roughness. This result was confirmed by angular-resolved X-ray photoemission measurements. Upon oxidation under the above conditions, the angular dependencies of the ratio of the oxidic Al^{3+} component intensity to that of metallic Al^0 component (not shown) could only be fit to a simulation assuming interface island formation.

5.2. Growth kinetics

As discussed in Section 4, the growth kinetics of an ultra-thin oxide layer can typically follow either a direct or an inverse logarithmic rate law. Experimentally, it is usually difficult to distinguish between direct and inverse logarithmic growth, because they result in very similar time dependencies for the oxide thickness, and the latter one is only an approximate solution to the growth equation. Besides, an accurate measurement of the oxide thickness by commonly used techniques requires well-defined values of some macroscopic thin film properties, namely optical parameters for ellipsometry or electron mean free path and sensitivity factors for photoelectron spectroscopy. Sometimes, analysis of the physical parameter values of a system assuming different rate laws can help in choosing between the different possible models [17,30]. For ion scattering, the scattering cross-sections are known with high precision. This allows an accurate measurement of the areal oxygen density from the O peak area, which can be converted into oxide thickness assuming the bulk density of Al_2O_3 (3.7 g/cm^3). Fig. 5(a) and (b) shows two presentations of the 573 K data from Fig. 2, aimed at determining the kinetic law that describes them better. A quantitative measure of
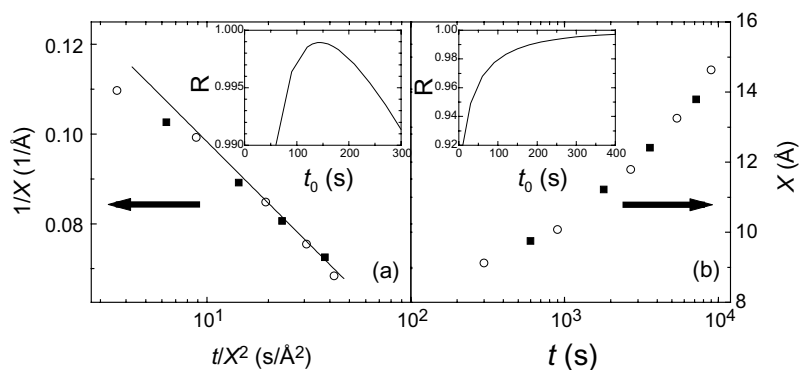
Fig. 5. Time dependence of Al_2O_3 thickness plotted as: (a) $1/X$ against $\ln(t/X^2)$, in order to test inverse logarithmic kinetics; (b) X against $\ln(t)$, to test direct logarithmic kinetics. Open and filled symbols correspond to two oxidation sequences. The insets show the correlation coefficient R for these data as a function of the time shift t_0, as described in the text. The straight line is the least-square linear regression for inverse logarithmic kinetics with $t_0 = 144$ s, corresponding to the maximum value for R.

the quality of the fit is the linear correlation coefficient R, which has a value of 1 when the data points lie on a straight line, and 0 if their x and y coordinates are not correlated. From a comparison of (a) and (b), the kinetic data can be better fit by the inverse logarithmic growth law. One should keep in mind, however, that an initial oxide thickness of 8 Å is ascribed to time $t = 0$. That explains the departure from linearity of the two points in Fig. 5(a) for smaller oxidation times, which are comparable with the time t_0 required to grow 8 Å of oxide starting with a clean surface. This time is less than 300 s for RT oxidation at 1×10^{-3} Torr, and can be expected to be much smaller at 573 K. For both data presentations, the linearity can be improved by introducing a time shift $t \rightarrow t + t_0$. Additionally, a similar shift $t \rightarrow t + \tau$ provides a better approximation to the solution of the Cabrera–Mott growth equation [31]. Insets to Fig. 5 show how the correlation coefficient changes with varying t_0 for both types of kinetics. For the inverse logarithmic dependence, R reaches a maximum value of 0.99893 at $t_0 = 144$ s. The least-square linear fit for this t_0 is shown by the solid line in Fig. 5(a). On the contrary, if the data are plotted as X against $\ln(t)$, a maximum in the correlation coefficient ($R = 0.99797$) is obtained at an unreasonably large time shift of about 600 s (see inset in Fig. 3(b)). Thus, the oxidation kinetics is better described by the Cabrera–Mott theory.

Assuming the validity of the inverse logarithmic law, the physical parameters for the Al_2O_3/Al system (N, W_0 and $\Delta\varphi$) have been derived from the least-square linear fits of Eqs. (2a)–(2c) to the data from Fig. 2. The values of $\Omega = 30.5$ Å^3 and $2a = 2.48$ Å are calculated from the alumina bulk density of 3.7 g/cm^3, and the charge for O ions is presumed to be $q = -2e$. The potential difference across the film in the temperature range of 573–673 K is found to be 0.8 ± 0.2 V. This result agrees well with the value of 0.73 V, reported for dry oxidation of aluminum foil at 1 Torr [32]. The corresponding value of the electric field in the oxide is ∼7 MV/cm. This is within the limits for the breakdown field of 3–13 MV/cm in thick anodic alumina film [33], which suggests good dielectric properties of the grown oxide film. The slope of the Arrhenius plot for u defines the barrier W_0 for ionic motion (or incorporation into oxide, whatever is larger) in the absence of a field: $W_0 = 1.67 \pm 0.13$ eV. This is in excellent agreement with the value of 1.60 eV, determined in an earlier study [32]. The concentration of the potentially mobile species on the interface, where defect injection occurs, is found from the intercept: $N = 2 \times 10^{(12\pm1)}$ cm^{-2}. Assuming an electrostatic field $E = 7 \times 10^6$ V/cm according to the evaluation above, the charge density at the gas–oxide and oxide–metal interfaces can be estimated from Gauss' theorem for the field across a flat capacitor: $N = \kappa\varepsilon_0 E/q$, where $\kappa = 9$ is the alumina dielectric

constant. The result of 1.7×10^{13} cm^{-2} falls in the concentration range obtained from kinetic data. This concentration is at least two orders of magnitude larger than that reported by others [19,32]. The obvious disagreement is reflected in the much faster oxidation rate observed in this work, as compared to other results [15,32]. To reconcile the controversy, we speculate that then enhancement in the oxidation rate may result from its dependence on crystallographic orientation. This might be expected if incorporation of migrating species (e.g. injection of oxygen vacancies into oxide) occurs at the oxide–metal interface. While previous kinetic studies have been concerned with oxidation of Al(1 1 1) or polycrystalline Al surface, in this work the open and defect-rich Al(1 1 0) face has been used. This could account for a larger number of species available for migration in this case. A detailed study of oxidation kinetics on Al(1 1 1) and Al(1 0 0) faces is required to confirm this assumption. These closely packed faces with a more perfect structure can be expected to generate a smaller number of Al species available for the formation of new oxide bonds, decreasing the rate of formation of interface oxygen vacancies. The effects of modification of the oxide structure by water contamination can also not be excluded.

Another piece of evidence favoring inverse logarithmic kinetics comes from the analysis of the evolution of the oxygen peaks with increasing oxygen exposure, summarized in Fig. 6. At 473 K the re-oxidant (tracer) peak slowly broadens as oxidation proceeds, but at all exposures it remains narrower than the marker peak. The width of the marker peak is also affected by oxidation. It increases at about the same rate as that of the tracer. At the higher oxidation temperature (573 K), the widths of the oxygen peaks become approximately equal, and increase with the same rate as the oxide grows. Finally, as seen from Fig. 6(c), for oxidation at 673 K the rate of the broadening is larger for the tracer signal, and it becomes wider than the marker signal. The width of the marker peak eventually becomes almost constant at the highest exposures. Marker film broadening during oxidation reflects the increase in the width of the marker depth distribution. In other words, the oxygen species from the marker oxide are affected by the
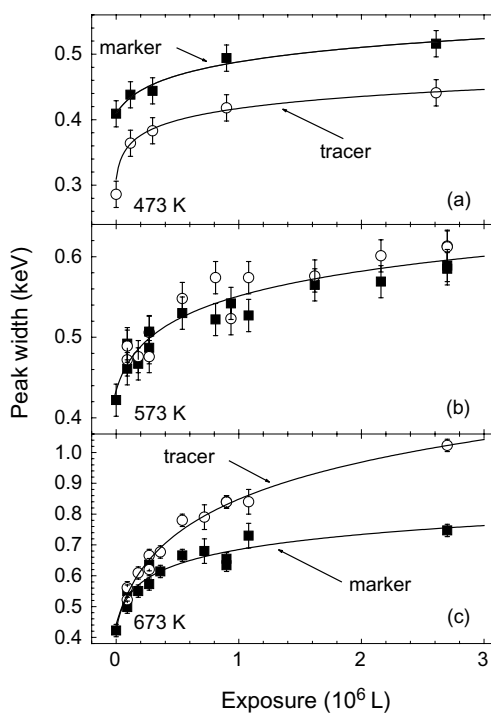
Fig. 6. Variation of the oxygen peak widths with exposure for oxidation at (a) 473 K; (b) 573 K; (c) 673 K. Filled squares correspond to the marker (first step oxidant), and open circles to the tracer (re-oxidant). Data are obtained at both fixed pressure of 3×10^{-4} Torr and fixed oxidation time of 15 min. Solid lines are logarithmic fits to guide the eye.

re-oxidant, pushing them away from the surface. Oxygen transport along extended defects (characteristic of direct logarithmic kinetics) or by jumps from an interstitial site to another (adjacent) interstitial site would keep the marker oxide, and hence the relevant oxygen peak width, unchanged. On the other hand, in the place exchange (interstitialcy) mechanism an interstitial ion injected at the interface knocks out a network atom, forcing it to become an interstitial and subsequently to replace the next network atom, and so on. This mechanism, as well as oxygen migration by vacancy movement would result in a broadening of the marker distribution. Therefore, we associate the observed marker peak broadening with oxygen transport by means of point defects jumps, characteristic for inverse logarithmic kinetics. Thus, both the kinetic data and the oxygen redistribution in the film upon re-oxidation confirm the Cabrera–

Mott mechanism with inverse logarithmic growth kinetics.

Additional information about the microscopic growth mechanism can be extracted, at least in principle, from the oxide growth rate as a function of oxygen pressure. This dependence is expected to be different when defect injection occurs at the gas–oxide (oxygen interstitials or metal vacancies) and oxide–metal (oxygen vacancies or metal interstitials) interfaces. In the both cases, the gas pressure determines the concentration of oxygen ions on the oxide surface (which are assumed to be in equilibrium with the gas phase in this P–T–t range) and thus the magnitude of the electric field across the film, lowering the activation barrier for the injection and transport of the migrating species. A dependence of the surface electrostatic potential on pressure is evident from the measurements of contact potential [34]. If injection takes place at the gas–oxide interface, an additional contribution to the pressure dependence of the growth rate arises because in this case the pressure controls not just the barrier for defect incorporation into oxide, but also the number of species available for this incorporation. Unfortunately, the change in the oxidation kinetics emerging from this contribution is too small to allow an experimental distinction between these two cases. Fig. 7 shows the oxygen uptake in the oxide versus pressure during re-oxidation (for 15 min in $^{16}O_2$) of an 8 Å thick Al_2O_3 layer. The change in the O areal density corresponds to the
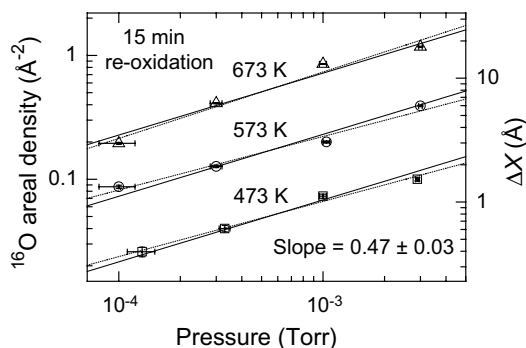
Fig. 7. The pressure dependence of the oxide thickness increment during re-oxidation. The straight solid lines have a slope of 1/2. The dashed lines are the least-square linear fits with an average slope of 0.47 ± 0.03.

oxide growth rate integrated over 15 min. A reasonable fit by a straight line with a slope of 0.5 (solid) supports a parabolic pressure dependence of the growth rate, in agreement with previous work [15,34]. The best linear fits are shown by the dashed lines. The slope, averaged over all data, is 0.47 ± 0.03, in agreement with parabolic pressure dependence.

5.3. Profiling of $^{16}O/^{18}O$ tracers in the oxide film

The analysis above of the integrated peak characteristics provides kinetic and structural information. A consideration of the evolution of the peak widths also reveals some features of the microscopic processes involved in the material transport across the film during oxidation. This section will deal with a more accurate analysis of the evolution of the peak shape, achieved by simulation of the MEIS spectra by modeling the elemental depth distributions. Some important qualitative observations can be made by visual examination of the peak shape. Fig. 8 compares the energy spectra for the aluminum oxide film before (a) and after (b) re-oxidation at 3×10^{-4} Torr for 120 min. The latter film consists of 57% of ^{16}O and 43% of ^{18}O. The leading edge positions for both oxygen peaks coincide with the backscattered proton energy calculated for the nuclei located at the surface. Also, the two oxygen peaks have the same width. These two facts imply that the oxygen isotopes are intermixed throughout the film. However, the peak shapes are clearly different, indicating a variation of the oxygen isotopic ratio across the film. A difference spectrum of the two spectra in Fig. 8(a) and (b) is shown in Fig. 8(c). The presence of both negative and positive contributions in the ^{16}O peak reflects the displacement of the marker ^{16}O from the surface deeper into the film, caused by ^{18}O incorporation during re-oxidation. The areas of the negative and positive parts are equal. Thus, no oxygen loss from the film occurs during oxidation at 573 K. Quantitative information can be obtained by numerical deconvolution of the peaks. First we outline the depth distribution model for the simulation. We then discuss the time evolution of the depth profiles during re-oxidation.
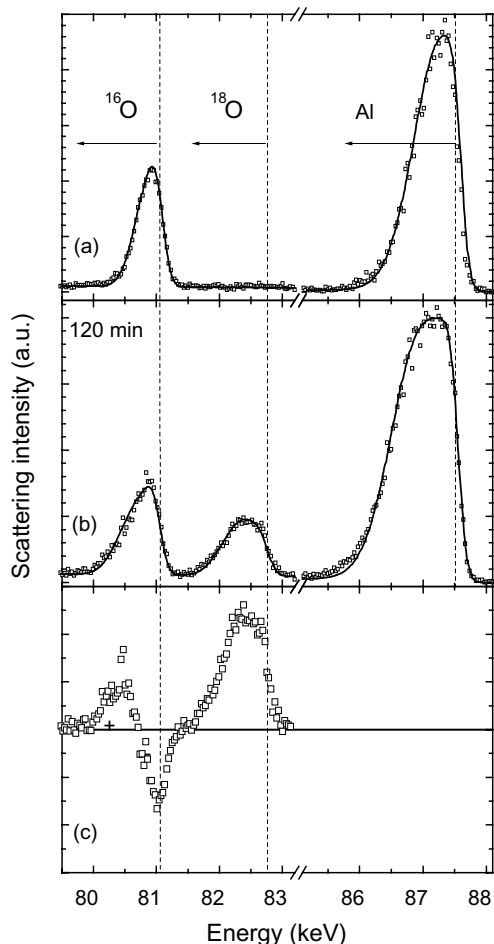
Fig. 8. Energy spectra for protons scattered from: (a) Al(1 1 0) oxidized in $^{16}O_2$ at RT during 30 min, pressure 1×10^{-3} Torr; (b) the same specimen re-oxidized in $^{18}O_2$ at 573 K during 120 min, pressure 3×10^{-4} Torr. Vertical dashed lines indicate the calculated positions for backscattering from surface atoms of ^{16}O, ^{18}O and Al. The solid line is the best fit to the experimental data shown by the open symbols, simulated using depth profiles for Al, ^{18}O and ^{16}O from the Fig. 9. The difference spectrum in the oxygen region for the spectra in (a) and (b) is shown in panel (c). The negative peak at the surface position for the ^{16}O isotope implies displacement of the marker oxygen from the surface deeper into oxide.

5.3.1. Model for the oxygen distribution in the oxide film

As we have shown in the Section 5.1, the oxide film has a stoichiometric composition and a relatively sharp (with respect to the thickness) interface. Therefore, in the model we assume a constant
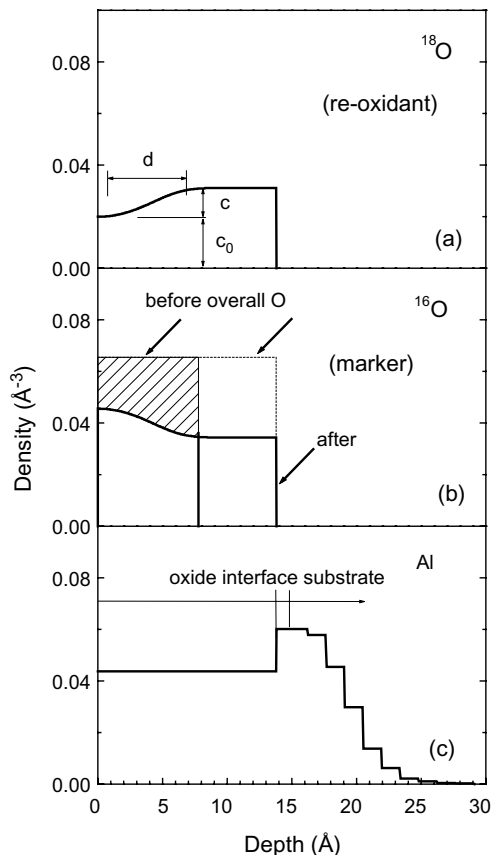
Fig. 9. The depth distributions for (a) ^{18}O, (b) ^{16}O, and (c) Al, used to simulate the energy spectra in Fig. 8. The values of c_0, d and δc define the oxygen profile shape according to Eq. (4). The dashed line in panel (b) corresponds to the total concentration of the two O isotopes, the rectangle (solid line) is the ^{16}O profile before re-oxidation, and the shadowed area indicates the net amount of ^{16}O that has moved during re-oxidation.

overall oxygen concentration inside the film, and an abrupt oxide boundary with the substrate, as shown by the dashed line in Fig. 9(b). This concentration corresponds to the density of bulk alumina and has a value of 0.0655 Å^{-3}. The overall O areal density, calculated from the peak areas, determines the boundary position (and oxide thickness). The tracer (re-oxidant) depth profile across the film, $n_t(z)$, where z is the coordinate perpendicular to the surface, can be conveniently described by the expression

$$n_t(z) = c_0 + (-1)^k \cdot \delta c \cdot \mathrm{erf}^k \left(\frac{z}{d} \right), \quad k = 1, 2, \quad (4)$$

which covers a broad range of concentration profile shapes (erf denotes the error function). The meaning of the variables c_0, δc and d is clear from Fig. 9(a), which depicts the re-oxidant distribution modeled by Eq. (4) with $k = 2$. The value of c_0 defines the surface concentration of the re-oxidant, δc is the gradient between the surface and interface concentrations, and d is the width of the transition region. For $k = 1$ and $c_0 = \delta c$ we obtain a solution to the diffusion equation with a constant surface concentration for the diffusing species. The marker (first oxidant) distributions after the first and the second oxidation stages are shown in Fig. 9(b) by solid lines. It is defined as $n_m(z) = 0.0655 - n_t(z)$. One can clearly see a significant movement of the marker species, forced by the new oxide growth.

Finally, the Al profile is sketched in Fig. 9(c). The aluminum atomic density within the oxide has been given its stoichiometric value of 0.0437 Å^{-3}. The excess interface Al (see Section 5.1) has been formally accounted for by introducing an additional 1 Å-thick layer of Al with a density of 0.0602 Å^{-3}. The Al substrate is modeled by a step-like structure, each step corresponding to one atomic layer of the substrate. The step width (1.432 Å) is equal to the interlayer separation for the Al(1 1 0) surface. The step height corresponds to the fraction of that layer visible to the detector in the scattering geometry used for the measurements. It is obtained by a complete-crystal Monte–Carlo simulation [35] for the clean Al(1 1 0) surface. Optimization of the crystal structure/ dynamics parameters by fitting the angular scattered yield gave the values for relaxation in the first and second interlayer distances of −8.5% and +5.4%, respectively, in a good agreement with previous studies [36–38], and 1-d rms vibrational amplitudes enhanced by 90% in the first and 50% in the second layer compared to the bulk value (0.105 Å [39]). Using these values we obtain a predicted yield of 0.302 Å^{-2} in the blocking direction, in good agreement with experiment for the clean surface. Though the presence of an oxide layer can be expected to modify the relaxation and vibration amplitudes of the interface substrate atoms, we did not observe a significant change in the shape of the angular scattering yield upon oxidation. Therefore, we adopted the profile obtained for the visible atoms in the clean Al(1 1 0) substrate in all simulations.

Provided the elemental depth profiles are known, the backscattering energy spectra can be calculated following the standard procedure [40]. The electronic stopping power in the oxide, which determines the proton energy loss in the target, was found from the semi-empirical energy dependencies for elemental stopping powers [41] using Bragg's rule. The stopping power in the substrate was adjusted to take into account the higher electronic density along the proton trajectories in the vicinity of the atomic strings, by using this density as the only fitting parameter for the clean Al(1 0 0) surface peak simulation. To include the statistical broadening of the proton energy distribution due to the random electronic scattering in the target (straggling) we used a Gaussian energy distribution (convoluted with the instrumental resolution). The standard deviation in the limit of high-energy ions interacting with free electrons was given by Bohr [42]. However, this approximation does not provide a satisfactory estimate of straggling for protons in the 100 keV energy range. Therefore we have applied more realistic values, obtained for the elemental targets in the framework of the Lindhard and Scharff formalism [43] based on the local electronic density approximation. Bragg's rule was used for straggling evaluation in alumina. The quality of the fit was defined by the rms deviation χ of the calculated spectra from the experimental ones. The three free parameters in Eq. (4) are constrained by the imposed restriction that the area under the tracer profile should be equal to the areal density calculated from the peak area. Thus, only c_0 and d in Eq. (4) have been varied independently. Their optimization has been performed by plotting contour plots of χ as a function of these parameters. The best fits to the spectra in Fig. 8(a) and (b) are shown by the solid line. The fit for the marker oxide before re-oxidation (Fig. 8(a)) is based on the marker oxygen profile shown as a solid line rectangle in Fig. 9(b). The shadowed area shows the net ^{16}O movement forced by the new oxygen incorporation. It is associated with the negative part of the ^{16}O peak in the Fig. 8(c).

5.3.2. Time dependence of the oxygen depth profiles

The rate limiting process for oxidation can be either interface defect incorporation or diffusion across the oxide. In the former case, the defect injection is followed by its rapid transport across oxide, resulting in a relatively sharp boundary between ^{18}O and ^{16}O distributions. If the migration across oxide is slow, the re-oxidant distribution will slowly broaden with time, increasing the tracer concentration at the oxide–metal interface.

The time evolution of the oxygen incorporation is presented in Fig. 10(a), which shows a set of the re-oxidant (^{18}O) profiles for two oxidation temperatures and several oxidation times. They are described by Eq. (4) with $k = 2$ and best-fit values for parameters c_0 and d. As re-oxidation begins, the tracer surface concentration quickly approaches the saturation level, which is maintained later at an approximately constant temperature-independent value. The re-oxidant preferentially incorporates in the interface region, rather than at the surface. Fig. 10(b) shows how the surface and interface ^{18}O concentrations change with oxidation time. While the surface concentration becomes only slightly larger, steady growth of the interface ^{18}O incorporation with time occurs. At 673 K, the interfacial tracer concentration eventually levels off slightly below the overall oxygen concentration in the oxide. After that, the ^{18}O distribution evolution is mostly restricted to propagation deeper into the substrate. The observed slow broadening of the tracer distribution is consistent with the

migration across the oxide being a kinetically rate-limiting process. This assumption was verified by a simple estimate of oxidation energetics. Overall (effective) activation energy W for oxidation (which is dependent on oxide thickness) was derived from the kinetic analysis in Section 5.2. This energy is determined by the larger of the activation barriers for oxygen defect incorporation W_i at one of the interfaces and for jumps between two sites within oxide W_d. On the other hand, an analysis of the tracer depth profiles can be employed to extract parameters explicitly defining the rate of the oxygen motion across the oxide film after its injection. The tracer peak shapes upon re-oxidation at 473 and 573 K for a short time (up to 15 min) could be simulated modeling the re-oxidant depth distribution by a complementary error function with the diffusion length d as a single fitting parameter (Eq. (4) with $k = 1$ and $c_0 = \delta c$). Assuming that the (classical) relationship $d = 2\sqrt{Dt}$ holds, the apparent diffusion coefficient D for the tracer atoms has been calculated at these temperatures (and for the same pressure as that used for kinetic studies). However, one should exercise care applying this expression because the diffusion equation is not valid for the strongly non-equilibrium system under consideration. Thus, use of D can be regarded rather as a simplified way to characterize the rate of oxygen motion. An Arrhenius plot of D provides an estimate of the activation energy W_d for an oxygen jump inside the film. In this way the energetics of defect incorpo-
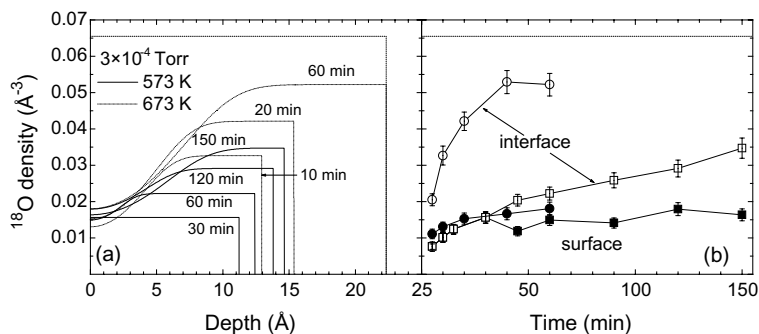
Fig. 10. (a) ^{18}O (re-oxidant) depth distributions upon oxidation at 3×10^{-4} Torr and temperature of 573 K (solid lines) and 673 K (dotted lines) for various times; (b) time dependence of the surface (filled symbols) and interface (open symbols) ^{18}O concentrations. Squares and circles correspond to 573 and 673 K, respectively. Dashed lines in both panels show the overall O concentration in oxide layer.

ration and migration can be separated. If W is larger than W_d, then overcoming the surface or interface barrier is the rate-limiting step for oxidation, and surface/interface processes define its rate. If W is equal to W_d, the rate-limiting step is O movement within oxide, as we assumed from the above consideration of the time evolution of the re-oxidant distribution in the film. Our estimate for the diffusion activation barrier at an oxide thickness of ~ 10 Å gives $W_d \approx 1.3 \pm 0.3$ eV, which compares well with $W = 1.47$ eV from kinetic data. Therefore we conclude that oxygen movement inside the oxide is the likely rate-limiting step during oxidation.

5.3.3. Surface exchange reaction

A surface exchange reaction is an incorporation of oxygen from the gaseous phase into the oxide by replacement of the surface network oxygen. If this reaction is accompanied by release of the network oxygen into the gaseous phase, it does not contribute to the oxide growth. Therefore, care needs to be exercised, if the oxidation kinetics is evaluated from the ^{18}O amount incorporated into the ^{16}O-formed film. In the case of Si oxidation, the fraction of surface-incorporated ^{18}O which contributes to oxide growth is less than 1% for 100 nm films, and increases for thinner films [44]. The rate of the surface exchange reaction can be linked to the concentration of surface active centers for defect incorporation or of potentially mobile species [45]. Thus, it is possible to relate oxygen exchange to the oxidation mechanism. The exchange reaction is expected to occur, if oxygen (rather than the metal) is the dominant migrating species. Oxygen loss from the ^{18}O-formed oxide film during further oxidation in $^{16}O_2$ can be directly measured by monitoring $^{18}O_2$ and $^{16}O^{18}O$ species in the gas phase [45]. In our work, the change in the marker signal in oxide was measured by MEIS.

The dependence of the marker concentration on the oxygen exposure during re-oxidation at various temperatures is shown in Fig. 11. Either ^{16}O (open symbols) or ^{18}O (filled symbols) was used to form the marker film. The re-oxidation exposure was varied by changing the oxidation time or the pressure. The data for 473 and 573 K are well fit with horizontal lines, indicating an absence of
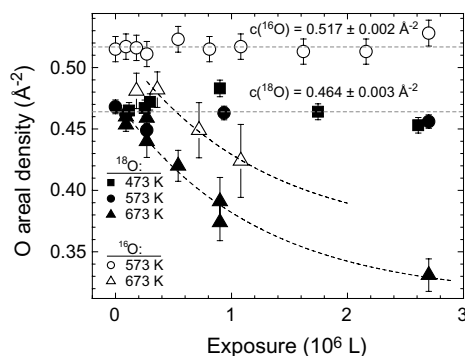
Fig. 11. Amount of marker oxygen isotope in the oxide after re-oxidation under different conditions. The marker oxides formed by ^{16}O and ^{18}O isotopes are shown by open and filled symbols, respectively. Dashed lines are drawn to guide the eye. The difference of about 0.06 Å^{-2} in the initial ^{16}O and ^{18}O concentrations corresponds to oxide initially formed by ^{16}O-containing impurities in $^{18}O_2$. The horizontal dashed lines imply that no oxygen loss takes place during oxidation at the temperatures up to 573 K.

oxygen loss into the gas phase. The average marker concentration is 0.517 Å^{-2} for the ^{16}O marker and 0.464 Å^{-2} for the ^{18}O marker. The difference is due to the fact that a fraction of the $^{18}O_2$-grown marker film is formed by ^{16}O-containing impurities. From Fig. 11, an exchange reaction between the oxide and the gaseous oxygen molecules is detected at 673 K, since some of the initially present oxygen is removed from the film. At the highest exposure of 2.7×10^6 L at this temperature, 10% of ^{16}O incorporated in the oxide during the second oxidation step, was simply exchanged with ^{18}O; in this case, 30% of the original ^{18}O amount left the film. The observation of the exchange reaction only at elevated temperatures can be attributed to a high activation barrier for this reaction. Another important factor is the lowering of the electric field across the oxide for thicker films grown at higher temperatures. At 573 K, the oxide thickness did not exceed 15 Å, and thus the gradient of the electric field across the oxide is large, resulting in the potential barrier for an inward oxygen jump being much smaller than for an outward jump. This prevents oxygen, already fixed in the oxide, from moving into the gaseous phase. When the oxide becomes thicker, the barrier for the outward movement is reduced due to the lower

field, and a non-negligible probability of escaping into the gas phase exists.

6. Conclusions

In summary, we have presented an MEIS study of the thermal oxidation of Al(1 1 0) in the regime of continuous Al_2O_3 film formation. At temperatures up to 573 K we observe growth of the planar stoichiometric oxide film. A roughness onset was detected at 673 K. Kinetic data are consistent with the Cabrera–Mott oxidation mechanism. Sequential $^{16}O_2$, then $^{18}O_2$, oxidation shows preferential incorporation of re-oxidant near the oxide–metal interface at prolonged oxidation times, accompanied by a redistribution of the network oxygen in the original oxide. We regard that as evidence of the oxygen species being the major contributor to the material transport across the oxide film. Our interpretation of the isotopic substitution results suggests rapid interface formation of oxygen defects and their subsequent slow migration across the oxide overlayer. The latter is a rate-limiting process controlling oxidation reaction. Some oxygen loss into the gaseous phase was observed only at the highest oxidation temperature used. Our results demonstrated that MEIS is able to reveal oxygen depth distribution details on a sub-nm scale.

Acknowledgements

References

[1] N. Cabrera, N.F. Mott, Rep. Prog. Phys. 12 (1948 – 1949) 163.
[2] G.L. Hunt, I.M. Ritchie, Oxid. Met. 2 (1970) 361.
[3] H.D. Ebinger, J.T. Yates, Phys. Rev. B 57 (1998) 1976.
[4] V. Zhukov, I. Popova, J.T. Yates, Phys. Rev. B 65 (2002) 195409.
[5] I. Popova, V. Zhukov, J.T. Yates, Surf. Sci. 518 (2002) 39.
[6] C. Ocal, S. Ferrer, N. Garcia, Surf. Sci. 163 (1985) 335.
[7] I. Popova, V. Zhukov, J.T. Yates, Phys. Rev. Lett. 89 (2002) 276101.
[8] I. Popova, V. Zhukov, J.T. Yates, Langmuir 16 (2000) 10309.
[9] A. Atkinson, Rev. Mod. Phys. 57 (1985) 437.
[10] F.P. Fehlner, N.F. Mott, Oxid. Met. 2 (1970) 59.
[11] K.R. Lawless, Rep. Prog. Phys. 37 (1974) 231.
[12] J.A. Davies, B. Domeij, J.P.S. Pringle, F. Brown, J. Electrochem. Soc. 112 (1965) 675.
[13] F. Brown, W.D. Mackintosh, J. Electrochem. Soc. 120 (1973) 1096.
[14] R.K. Hart, J.K. Maurin, Surf. Sci. 20 (1970) 285.
[15] B.E. Hayden, W. Wyrobisch, W. Oppermann, S. Hachicha, P. Hofmann, A.M. Bradshaw, Surf. Sci. 109 (1981) 207.
[16] T. Do, N.S. McIntyre, Surf. Sci. 440 (1999) 438.
[17] T. Do, S.J. Splinter, C. Chen, N.S. McIntyre, Surf. Sci. 387 (1997) 192.
[18] F.P. Fehlner, Low Temperature Oxidation: The Role of Vitreous Oxides, John Wiley & Sons, New York, 1986.
[19] J. Grimblot, J.M. Eldridge, J. Electrochem. Soc. 129 (1982) 2369.
[20] A. Jimenéz-Gonzaléz, D. Schmeisser, Surf. Sci. 250 (1991) 59.
[21] L.P.H. Jeurgens, W.G. Sloof, F.D. Tichelaar, E.J. Mittemeijer, Phys. Rev. B 62 (1999) 4707.
[22] J.F. van der Veen, Surf. Sci. Rep. 5 (1985) 199.
[23] R.M. Tromp, M. Copel, M.C. Reuter, M.H. von Hoegen, J. Speidell, R. Koudijs, Rev. Sci. Instrum. 62 (1991) 2679.
[24] D. Semrad, P. Bauer, Nucl. Instr. Meth. Phys. Res. B 12 (1985) 24.
[25] G. Molière, Z. Naturforsch. 2a (1947) 133.
[26] D.J. O'Connor, E.R. Wouters, A.W.D. van der Gon, J.F. van der Veen, P.M. Zagwijn, J.W.M. Frenken, Surf. Sci. 296 (1993) 131.
[27] J.A. Phillips, Phys. Rev. 97 (1955) 404.
[28] H.C. Lu, E.P. Gusev, E. Garfunkel, T. Gustafsson, Surf. Sci. 351 (1996) 111.
[29] C.J. Dell'Oca, L. Young, Appl. Phys. Lett. 13 (1968) 228.
[30] F.P. Fehlner, J. Electrochem. Soc. 131 (1984) 1645.
[31] R. Ghez, J. Chem. Phys. 58 (1973) 1838.
[32] M.J. Dignam, W.R. Fawcett, H. Böhni, J. Electrochem. Soc. 113 (1966) 656.
[33] N. Klein, M. Albert, J. Appl. Phys. 53 (1982) 5840.
[34] C.T. Kirk, E.E. Huber, Surf. Sci. 9 (1968) 217.
[35] J.W.M. Frenken, R.M. Tromp, J.F. van der Veen, Nucl. Instr. Meth. Phys. Res. B 17 (1986) 334.
[36] J.R. Noonan, H.L. Davis, Phys. Rev. B 29 (1984) 4349.
[37] J.N. Andersen, H.B. Nielsen, L. Petersen, D.L. Adams, J. Phys. C: Solid State Phys. 17 (1984) 173.
[38] B.W. Busch, T. Gustafsson, Surf. Sci. 415 (1998) L1074.
[39] D.S. Gemmell, Rev. Mod. Phys. 46 (1974) 129.
[40] E.P. Gusev, H.C. Lu, T. Gustafsson, E. Garfunkel, Phys. Rev. B 52 (1995) 1759.
[41] H.H. Andersen, J.F. Ziegler, The stopping and ranges of ions in matter, vol. 3, Pergamon, New York, 1977.
[42] N. Bohr, Mat. Fys. Medd. Dan. Vid. Selsk. 18 (1948) 8.
[43] J. Lindhard, M. Scharff, Mat. Fys. Medd. Dan. Vid. Selsk. 27 (1953) 15.
[44] I. Trimaille, S. Rigo, Appl. Surf. Sci. 39 (1989) 65.
[45] T. Åkermark, Oxid. Met. 50 (1998) 167.